Poleward migration of the latitude of maximum tropical cyclone intensity – forced or natural?

Submitted for peer review.

Jonathan Lin,[a,b] Chia-Ying Lee,[a] Suzana J. Camargo,[a] Adam Sobel,[a,c]

[a] *Lamont-Doherty Earth Observatory, Columbia University, Palisades, NY*
[b] *Department of Earth and Atmospheric Sciences, Cornell University, Ithaca, NY*
[c] *Department of Applied Physics and Applied Mathematics, Columbia University, New York, NY*

ABSTRACT: Past studies have shown a significant observed poleward trend in the latitude at which tropical cyclones reach their lifetime maximum intensity (LMI), especially in the Northwest Pacific basin. Given the brevity of the historical record, it remains difficult to separate the forced trend from internal variability of the climate system. A recently developed tropical cyclone downscaling model is used to downscale the Community Earth System Model 2 (CESM2) pre-industrial control simulation. It is found that the observed trend in the latitude at which tropical cyclones reach their LMI in the Northwest Pacific is unlikely to be caused by internal variability. The same downscaling model is then used to downscale CESM2 simulations under historical forcing. The resulting trends distribution shows significant poleward migration of tropical cyclone LMI, even after regressing out the internal variability, as well as the effects of the forced signal that projects onto internal variability. The results indicate that the observed poleward migration of the latitude at which tropical cyclones reach their LMI in the Northwest Pacific basin is likely to be at least in part forced. However, the magnitude of the projected poleward trend in climate models can be significantly modulated by the simulated spatial pattern of ocean warming. This highlights how discrepancies between models and observations, with regards to projected changes to the equatorial zonal sea-surface-temperature gradient under anthropogenic forcing, can also lead to large discrepancies in projected changes to the LMI latitude of tropical cyclones.

SIGNIFICANCE STATEMENT: Observations in the Northwest Pacific basin show that the latitude at which tropical cyclones are at their most intense has been trending northwards in the recent half-century. These changes are important since tropical cyclones could bring hazardous weather to coastal areas that are poorly equipped to handle them. Here, we show that natural variations in Earth's climate are very unlikely to explain the observed poleward trend in the latitude that tropical cyclone reach their maximum intensity. We find that it is much more likely that the observed trend is forced by human-related emissions, though the spatial pattern of warming in response to greenhouse emissions can have significant impacts on the magnitude of the trend.

1. Introduction

Tropical cyclones (TCs) are dangerous weather systems that bring extreme wind, rain, storm surge, and flooding to coastal areas. In general, TCs form in the tropics, and move westward and poleward as they evolve over time. A number of observational and modeling studies argue that, as the planet warms from anthropogenic greenhouse gas emissions, TC activity has and will migrate poleward (Kossin et al. 2014, 2016; Sharmila and Walsh 2018; Daloz and Camargo 2018; Studholme et al. 2022; Lin et al. 2023a).

It is not easy, however, to quantify whether or not TC activity has expanded poleward over the historical period, given its brevity, as well as the lack of high-quality observational data. One metric that has been used to quantify TC activity is the latitude at which a TC attains its lifetime maximum intensity (LMI), deemed the latitude of lifetime maximum intensity (henceforth, ϕ_{LMI}). As noted in Kossin et al. (2014), ϕ_{LMI} is particularly useful because it (1) accounts for heterogeneity across basins in definitions of TC intensity, and (2) is less prone to past observational uncertainties. Research has shown that the global ϕ_{LMI} is moving polewards at $\approx 0.1^\circ$ per decade, most of which is due to TCs that occur in the Northwest Pacific basin (Kossin et al. 2014).

While there is a pronounced poleward trend in ϕ_{LMI}, it has occurred alongside natural interannual and decadal variability, which has been known to modulate many aspects of TC behavior, including ϕ_{LMI}. In the Northwest Pacific basin, two dominant modes of variability on these time scales are El Niño-Southern Oscillation (ENSO), and Pacific decadal variability (PDV) [see Capotondi et al. (2020) for discussion on this nomenclature]. In El Niño events, the mean genesis location of TCs shifts southeastward, while in La Niña events, it shifts northwestward (Chan 1985; Chia and Ropelewski 2002; Camargo et al. 2007a). PDV also exhibits similar controls on TC genesis, though comparatively smaller in magnitude (Song and Klotzbach 2018; Zhao et al. 2022). Furthermore, during El Niño, TCs tend to spend more time over warmer waters, leading to longer lifetimes (Wang and Chan 2002; Camargo and Sobel 2005) and stronger intensities (Camargo and Sobel

Corresponding author: Jonathan Lin, jonathanlin@cornell.edu

2005) [and vice-versa during La Niña]. ENSO is also known to significantly modulate the landfall locations of TCs (Saunders et al. 2000; Camargo et al. 2007b). Note, while there are other modes that affect TC behavior in the Northwest Pacific, such as the Pacific Meridional Mode (PMM) (Chiang and Vimont 2004; Zhang et al. 2016), in this work, we focus on ENSO and PDV. Early work on the PMM suggests that the PMM is a route through which extratropical variability can influence tropical variability (Chiang and Vimont 2004). Recent work, however, has highlighted the bi-directional coupling between ENSO and PMM (Stuecker 2018). Thus, the degree to which ENSO and PMM are independent is still an unsettled issue.

In many studies, natural internal variability has been recognized to contribute to the poleward trend in ϕ_{LMI} (Kossin et al. 2014; Moon et al. 2015; Song and Klotzbach 2018; Zhao et al. 2022). However, these same studies have debated over the relative roles of global warming and internal variability in the observed poleward trend in ϕ_{LMI}. Kossin et al. (2014) found that internal variability does not significantly contribute to the poleward trend in ϕ_{LMI}, and put forth a potential explanation for the observed poleward shift in ϕ_{LMI}: global warming meridionally expands regions that are favorable for TC formation and intensification. In contrast, Moon et al. (2015) emphasized that internal variability has a large influence on ϕ_{LMI} variability, contesting the findings of Kossin et al. (2014). Nearly a decade later, there is still a strong observed poleward trend in ϕ_{LMI} in the Northwest Pacific (see Figure 1), suggesting that global warming leads to a poleward expansion of ϕ_{LMI}. Nevertheless, the role of internal variability should not be downplayed; in this perspective, as suggested by Song and Klotzbach (2018), historical trends in ϕ_{LMI} are a function of both (1) interdecadal fluctuations in the genesis latitude that are related to internal variability, and (2) global warming induced trends that lead to a poleward expansion of ϕ_{LMI} (Kossin et al. 2014).

What are the physical mechanisms behind the poleward trend in ϕ_{LMI}? Is TC genesis merely moving poleward, or are there systematic changes to TC motion that favor poleward expansion? Wang and Wu (2019) emphasized the importance of changes to the large-scale steering flow (i.e. the tracks themselves) when considering the historical trend in ϕ_{LMI}. In contrast, Daloz and Camargo (2018) emphasized the importance of the genesis latitude to trends in ϕ_{LMI}, and found a significant poleward trend in the genesis latitude of Northwest Pacific TCs associated with the trend in ϕ_{LMI}. More recently, Zhao et al. (2022) argued that on interannual time scales, ENSO and PDV have significant controls on the genesis latitude of Northwest Pacific TCs, and track shifts are much less important when considering trends in ϕ_{LMI}. However, unlike ϕ_{LMI}, genesis latitude is sensitive to the definition of the point of genesis, which makes genesis latitude trends subject to large observational uncertainties.

While there have been a number of studies focused on understanding trends of ϕ_{LMI} in the Northwest Pacific basin, it remains difficult to separate the confounding influence of internal variability of the climate system with the anthropogenically forced signal. Observational studies typically regress out the linear influence of internal variability to unmask the forced signal (Kossin et al. 2014; Moon et al. 2015; Song and Klotzbach 2018; Zhao et al. 2022). This method, however, ignores the "pattern effect" (Stevens et al. 2016) – namely that global warming need not be uniform in space, and can have large spatial variations, some of which could project onto the dominant patterns of interannual and interdecadal variability. For instance, observed trends show an enhanced tropical Pacific sea-surface temperature (SST) zonal gradient (i.e. a more "La-Niña like" SST pattern), and it is unlikely that this is a mere byproduct of internal variability (Coats and Karnauskas 2017; Seager et al. 2019). These issues, coupled with a dearth of high-quality observations of TCs, make it difficult to deduce how much anthropogenic warming has contributed to historical trends in ϕ_{LMI}.

In this study, we attempt to disentangle the contributions of anthropogenic forcing and internal variability to trends in ϕ_{LMI} of TCs in the Northwest Pacific basin. We use a recently developed TC downscaling model (Lin et al. 2023b) to understand the behavior of TCs in long-running simulations of Earth's pre-industrial climate, as well as in simulations under historical forcing. Section 2 describes the methods and data used in this study. Section 3 follows with analysis of TC behavior in a pre-industrial control climate. Section 4 then shows the results and interpretation from downscaling historical simulations. Finally, section 5 concludes this study with a summary and discussion.

2. Methods and Data

In this study, we use Community Earth System Model 2 (CESM2), NCAR's latest suite of climate and earth system models (Danabasoglu et al. 2020). We have chosen to use CESM2 since it has been shown to simulate ENSO and PDV relatively well in the 1000-year pre-industrial control simulation – the model is run from model years 0 to 1200, but the first 200 years are thrown away the atmosphere to reach a stationary climate (Capotondi et al. 2020). There are notable biases, however, related to the amplitude and diversity of El Niño. The amplitude of El Niño is about 30% larger than that in the observations, and is more focused in the central Pacific than the eastern Pacific (Capotondi et al. 2020). Since the pre-industrial and historical CESM2 simulations are run at a nominal horizontal resolution of 100-km, it is likely that TC are poorly represented owing to coarse grid spacing (Davis 2018).

We choose to downscale both the pre-industrial and historical CESM2 simulations, using the publicly available,

TC downscaling model developed in Lin et al. (2023b), which is a derivative of the MIT TC downscaling model (Emanuel 2006). On a high level, the model works by randomly seeding and evolving weak protovortices in space and time, following the method of Emanuel et al. (2008). The seeds are advected by the background environmental winds, and strengthen/weaken according to a pair of dynamical equations that describe the intensification rate of a TC in the presence of vertical wind shear, ocean mixing, among other processes (Emanuel 2017). A vast majority of the seeds dissipate, and only seeds that reach an intensity of at least 15 m s^{-1} are kept. The model has been shown to broadly reproduce the climatology and variability of TCs over the historical period (Lin et al. 2023b). The reader is referred to Lin et al. (2023b) for more details.

The downscaling model uses monthly averages of the 250- and 850-hPa horizontal winds, 600-hPa temperature and specific humidity, potential intensity, SST, and surface pressure. These are used to drive the model over the CESM2 pre-industrial control run during model years 200-1200. We downscale 900 tracks globally for every year, for a total of 900,000 tracks over the entire pre-industrial period. Around 30% of the global tracks occur in the Northwest Pacific. The ensuing results do not change if the sample set is reduced in size by half, suggesting that the sample size is sufficient.

The ENSO phase and magnitude is determined using the Niño-3.4 index, which is the average of the SST anomaly over the eastern and central Pacific regions, from 5°S-5°N, and from 170°W-120°W (Barnston et al. 1997). Henceforth, ENSO index refers to the Niño-3.4 index. We use the Hadley Centre Sea Ice and Sea Surface Temperature data set (HadISST), from 1870-2022, to compute the ENSO index (Rayner et al. 2003). SST anomalies are computed with respect to the 1981-2010 mean. To coincide with the peak of the TC season in the Northwest Pacific, the ENSO index is averaged from July to October (JASO). Following Mantua et al. (1997), PDV is defined as the leading empirical orthogonal function of North Pacific (20°N-60°N) SST anomalies which have the seasonal cycle removed. In the pre-industrial control simulations, PDV is computed over the entire simulation, while in the historical simulations, PDV is computed over a period where the anthropogenic forcing is relatively small (1850-1950). Since there is no seasonal cycle in the PDV index, we use an annual-averaged PDV to describe the PDV phase during each year. The results are insensitive to whether PDV is annually-averaged or averaged only over JASO.

In order to benchmark the model to historical observations, we also downscale the ECMWF Reanalysis v5 (ERA5) reanalysis, from 1979-2022 (Hersbach 2016). The reanalysis data is downscaled in the same manner as CESM2. Historical TCs in the Northwest Pacific basin are identified using the International Best Track Archive for Climate Stewardship (IBTrACS) dataset from 1979-2022 (Knapp et al. 2018). In both the observations and the downscaling model, we only consider storms whose lifetime maximum intensity exceeds 30 knots, for consistency between the two datasets. TC intensity is determined using the USA best-track estimates of intensity via the Joint Typhoon Warning Center.

3. Unforced Trends

Before downscaling the pre-industrial control simulation, we first show that the downscaling model adequately represents the climatology of ϕ_{LMI} in the Northwest Pacific basin. To do this, we downscale ERA5 reanalysis data, from 1979-2022, as in Lin et al. (2023b). Figure 1a shows the probability distribution of individual storm's ϕ_{LMI} in the Northwest Pacific basin. In general, the observed distribution of ϕ_{LMI} is within the sampling error of the historical observations, except for a peak in ϕ_{LMI} frequency around 18 degrees latitude.

Figure 1b shows interannual variability of the annually-averaged ϕ_{LMI} in observations and as modeled by the downscaled tracks. The correlation between the two is modest ($r = 0.36$), though the signal may be reduced because of sampling error, as will be elaborated on in the ensuing paragraph. The magnitude of the ϕ_{LMI} trend in the downscaling tracks (0.34° per decade) is slightly smaller than that of the observations (0.38° per decade). The observational trend, however, is slightly sensitive on the minimum LMI required for each storm; for instance, if we increase the minimum storm LMI from 30 knots to 35 knots, the ϕ_{LMI} latitude trend rises to 0.51° per decade. In contrast, the ERA5 ϕ_{LMI} trend is not sensitive to this minimum LMI threshold. Finally, the average annual ϕ_{LMI} in the downscaling model is biased slightly equatorwards (0.5° in latitude).

In the historical observations, there are around 28 TCs per year in the Northwest Pacific basin that achieve a LMI of at least 30 knots. In contrast, the downscaling model can produce a substantially larger number of synthetic storms given statistically similar large-scale conditions, but randomizes the initial genesis points in space and time. Because of the small sample size in the observations, some fraction of interannual variability in annually-averaged ϕ_{LMI} could be merely a function of stochasticity in the genesis timing and location of the TCs. The sampling error of the observational dataset should thus be taken into account.

To account for this sampling error, we randomly subsample (bootstrap) the downscaled TCs to the same size as the historical observations from 1979-2022. Around 30% of the 900,000 total tracks occur in the Northwest Pacific, such that there are a total of around 275 TCs to sample from every year of the pre-industrial control simulation.

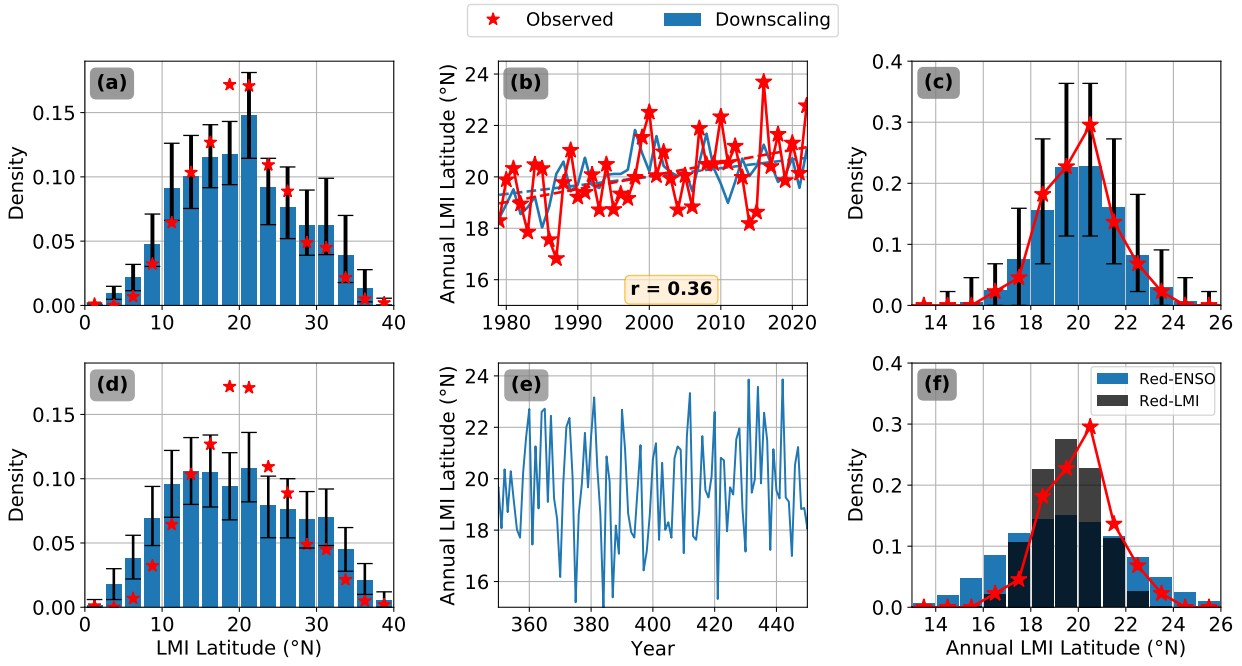

FIG. 1. **(a)** Distribution of individual storm ϕ_{LMI} in the Northwest Pacific basin, where error bars indicate the 95% confidence interval obtained by sub-sampling the ERA5 reanalysis downscaling events to the same size as the observational events. The observed distribution is shown in red stars. **(b)** Annually-averaged ϕ_{LMI} in the Northwest Pacific basin, as calculated from (red) observations, and (blue) the downscaled ERA5 tracks. **(c)** Distribution of annually-averaged ϕ_{LMI} in the (red) observations, and (blue) downscaling model with (black) 95% confidence intervals, after repeatedly sub-sampling the downscaling events to the observational count from 1979-2022. The bias of the downscaled annual ϕ_{LMI} (0.4°) is removed from the distribution. **(d)** Same as (c) but for CESM2. **(e)** The annually-averaged ϕ_{LMI} of downscaled TCs in the Northwest Pacific basin, over years 350-450 in CESM2. **(f)** Same as (c) but for Reduced-ENSO and Reduced-LMI.

We repeat this bootstrapping process 1000 times, and average the storm LMI for every year, creating 1000 samples of annual ϕ_{LMI}, for each year from 1979-2022. Figure 1c shows the distribution of annual ϕ_{LMI} in the downscaling model, along with 95% confidence intervals that represent the range of the annual ϕ_{LMI} distribution over a 44-year period (i.e. same size as the observational record). The small bias in ϕ_{LMI} is removed in Figure 1c in order to directly compare the variability about the mean. In general, we observe that the distribution of annual ϕ_{LMI} in the observations is within that of the downscaling model, especially when accounting for sampling errors. This gives confidence that the downscaling model can be used to estimate ϕ_{LMI}, given the large-scale environmental conditions.

We now proceed with analysis of the downscaled TCs from CESM2. Figure 1d shows the ϕ_{LMI} distribution for individual storms, throughout the 1000-year CESM2 period that was downscaled. The observed distribution, as well as the 95% confidence intervals of the downscaled distribution, are shown for comparison purposes. The downscaled distribution of ϕ_{LMI} qualitatively matches that of the observed distribution, though the frequency of ϕ_{LMI} from 15°N-25°N is less than that in the observations. This could potentially be caused by biases in the climate model mean-state, though that was not thoroughly investigated here. We do not expect the two to match exactly, however, since the large-scale environmental conditions are not exactly the same.

As an example, Figure 1e shows the annually-averaged ϕ_{LMI} of downscaled TCs in the Northwest Pacific basin, from years 350-450. The annual ϕ_{LMI} is obtained by averaging over all downscaled TCs, every year. Immediately obvious is that there is considerable interannual variability in the downscaled ϕ_{LMI}, which is exclusively a function of the interannual variability in the large-scale conditions. In fact, we qualitatively observe that there is an unforced poleward trend in ϕ_{LMI} in the 40-year time period from ≈390 to ≈430. The PDV phase is strongly positive from years 380-400, and almost exclusively negative from years 400-440 (see Fig. 17 of Capotondi et al. (2020)).

What is the sensitivity of ϕ_{LMI} to the modeled internal variability (ENSO and PDV)? Figures 2a,c show the distributions of the JASO-averaged ENSO and PDV indices. The interannual variability of the annual ϕ_{LMI} is much larger in the raw downscaling tracks as compared to observations, even when accounting for sampling variability (see Supplementary Figure S1). A large part of this is because the monthly amplitude of ENSO is about 30%

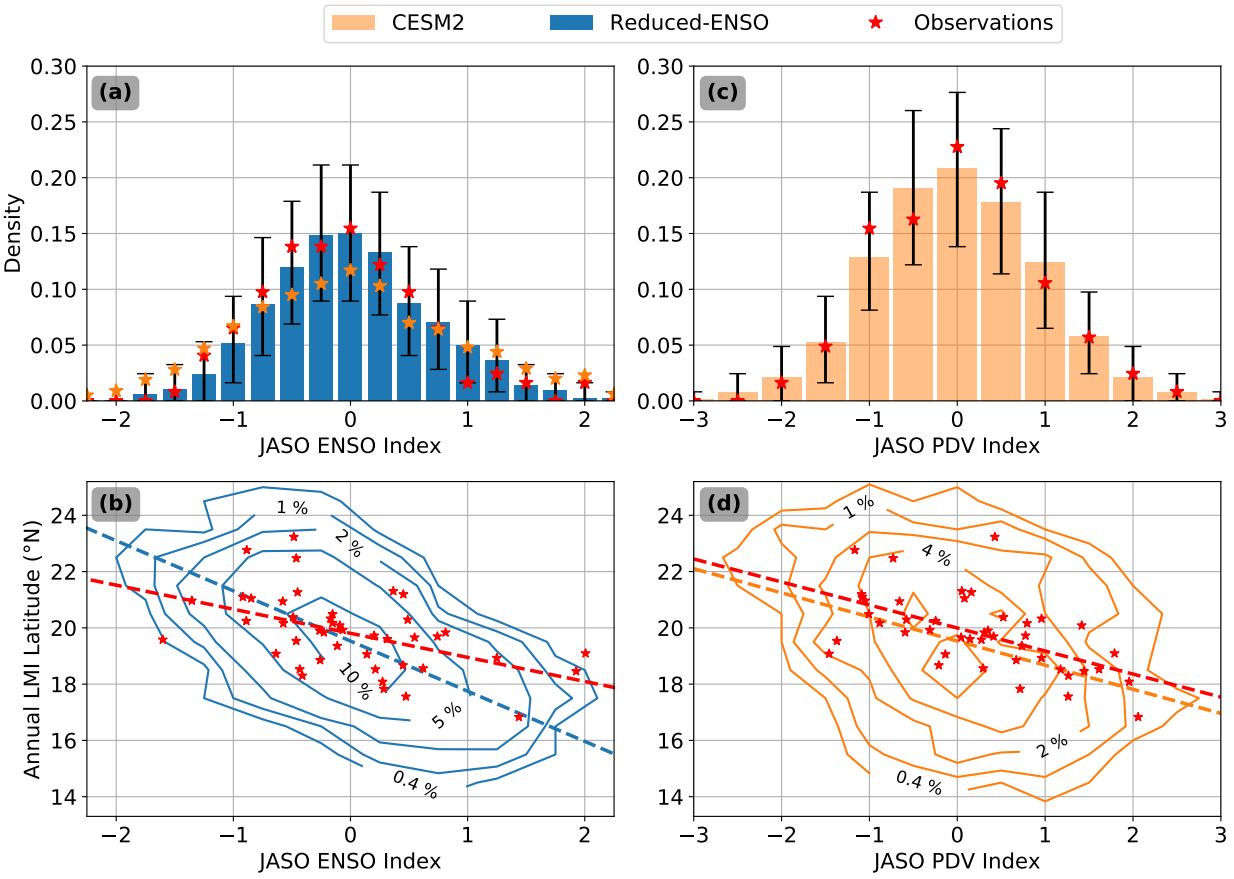

FIG. 2. **(a)** Probability distribution of the JASO ENSO index, in (red) observations, (orange) raw CESM2 fields, and (blue) the Reduced-ENSO case. 95% confidence intervals, obtained by sub-sampling the Reduced-ENSO case to the observational sample size, are shown. **(b)** Contour plots of the joint probability density distribution for JASO ENSO index, and the downscaled annual ϕ_{LMI} in the Northwest Pacific. Blue and red lines represent linear fits in the downscaling and observational data, respectively. **(c)** Same as (a), but for PDV of the uncorrected CESM2 fields. (**d**) Same as (b) but for the PDV.

stronger in CESM2 than in observations, as noted in Capotondi et al. (2020). Likewise, the amplitude of the JASO ENSO index in CESM2 is larger ($\approx 40\%$) than the observed JASO ENSO index, as seen in Figure 2a. Since this can significantly affect the magnitude of trends associated with internal variability, we reduce the magnitude of the JASO ENSO index in CESM2 by reducing its sample standard deviation (using 1 degree of freedom) to that of the observations. This amounts to dividing the JASO ENSO index of the CESM2 simulation by 1.41. These samples are denoted as "Reduced-ENSO", and are shown in Figure 2, along with the 95% confidence intervals that are obtained by sub-sampling the CESM2 ENSO index to the same sample size as observations. Note, the distribution of ENSO in the model is not expected to exactly match the observational distribution, since transient "La Niña"-like warming patterns may be associated with global warming (Coats and Karnauskas 2017; Seager et al. 2019).

Since there is a strong relationship between the JASO ENSO index and the downscaled annual ϕ_{LMI} ($r = -0.67$, shown by the dashed blue line in Figure 2b), a reduction in the magnitude of the ENSO events must also be accompanied by a reduction in the variability of annually-averaged ϕ_{LMI}. This is done by subtracting the product of (1) the sensitivity of ϕ_{LMI} to ENSO, and (2) the reduction in the magnitude of the CESM2 ENSO events (the bias correction), from the ϕ_{LMI} predicted by the downscaling model. This leads to interannual variations of ϕ_{LMI} in which the ENSO distribution is normalized to be similar to that in the observations. Note, the sensitivity of annual ϕ_{LMI} to ENSO is unchanged in the resulting ϕ_{LMI} distribution.

Figure 2b shows the joint probability density distributions between the bias-corrected Reduced-ENSO index and ϕ_{LMI}. While all of the observed pairs of JASO ENSO index and ϕ_{LMI} fall within the modeled distribution, the sensitivity (linear slopes) of ϕ_{LMI} to ENSO is larger in the downscaled tracks than in the observations, though within

2 standard errors of that of the observations. The stronger sensitivity in the downscaled CESM2 tracks could be because the CESM2 ENSO events have stronger amplitudes in the central Pacific, rather than in the eastern Pacific (Capotondi et al. 2020). The westward shift of SST variance could lead to overly strong controls of ENSO on ϕ_{LMI} in the Northwest Pacific basin.

Figure 1f shows the distribution of annual ϕ_{LMI}, for the Reduced-ENSO case. Even after correcting for the ENSO amplitude bias, we observe that the variability in annual ϕ_{LMI} is larger than in observations (owing to the larger sensitivity of ϕ_{LMI} to ENSO). While the two distributions do not necessarily have to be equal, we create a second set of bias-corrected samples, denoted "Reduced-LMI", as shown in Figure 1f. The Reduced-LMI samples are created by reducing the standard deviation of the annual ϕ_{LMI} distribution to be equal to that over the ERA5 downscaled historical period (1979-2022). Thus, the sensitivity of ϕ_{LMI} to ENSO is reduced (in this case, by $\approx 40\%$), and the variance of annual ϕ_{LMI} is roughly equal with that of the observations. The Reduced-ENSO and Reduced-LMI cases are two, more-or-less realistic estimates of ϕ_{LMI} variations that are only caused by internal variability.

The probability distribution of the annual PDV index is well-matched between CESM2 and the observations, as shown in Figure 2c, such that we do not modify the PDV index. This choice, however, is made despite the fact that PDV and ENSO are not independent modes of variability. In fact, their respective monthly indices are decently correlated ($r = 0.32$). Thus, in theory, reductions in ENSO amplitude must also be associated with reductions in PDV amplitude. In practice, this makes a little difference, since corresponding reductions in PDV amplitude reduce the standard deviation of the PDV index by only 5%. Note the sensitivity of ϕ_{LMI} to PDV is nearly the same in the CESM2 downscaled TCs as compared to that in the observations, as shown in Figure 2d.

We now evaluate the likelihood of the observed ϕ_{LMI} trend in a climate that has no anthropogenic forcing. Figure 3 shows the probability distribution and exceedance probability distribution of 44-year trends in the Northwest Pacific ϕ_{LMI}, calculated from the downscaled 1000-year CESM2 pre-industrial control simulation. For comparison purposes, we also show the 44-year trends distribution obtained by downscaling ERA5, from 1979-2022. The spread in this distribution is obtained by sub-sampling the ERA5 downscaling event set to an annual-average of 28 storms per year, as is similarly done in the pre-industrial control case. For the Reduced-ENSO case, there is only a 10% chance of seeing a trend exceeding that in observations, while for the Reduced-LMI case, there is only a 1% chance. In both cases, it is unlikely that the present poleward trend in ϕ_{LMI} can be explained purely through natural variability of the climate system. In contrast, the observed ϕ_{LMI} trend sits nearly at the median of the ϕ_{LMI} trends distribution obtained through downscaling the ERA5 dataset. These results are consistent with other work that shows a poleward expansion of ϕ_{LMI} in past warm climates, such as the Eocene and Pliocene, and future warmer climates, in response to anthropogenic greenhouse gas emissions (Kossin et al. 2016; Studholme et al. 2022).

However, the spread in the ERA5 trends distribution, which is only a function of the sampling error, is much smaller than that of the Reduced-ENSO case, which additionally depends on the sampling of many states of the climate system. This implies that internal variability can still significantly modify trends in ϕ_{LMI} and mask the global warming signal, as suggested by Song and Klotzbach (2018). This issue will be further explored in the next section.

In general, what are the processes that control the LMI trend in the downscaling model? Indeed, composites analyses show that both ENSO and PDV significantly modulate track density [Supplementary Figures S2-S3]. The LMI trend can be linearly decomposed into trends in the genesis latitude and trends in the TC tracks (Song and Klotzbach 2018; Zhao et al. 2022):

$$\Delta\phi = \phi_{\mathrm{LMI}} - \phi_{\mathrm{g}} \tag{1}$$

where ϕ_{g} is the genesis latitude, and $\Delta\phi$ roughly represents changes in TC tracks. The decomposition of each of these quantities to ENSO and PDV are detailed in Table 1. Here, we observe that ENSO is a large modulator of ϕ_{g} ($r = -0.75$) and ϕ_{LMI} ($r = -0.75$) , and less so, but still significantly for $\Delta\phi$ ($r = -0.5$). ϕ_{g} and ϕ_{LMI} are less sensitive to the PDV phase, with weaker but still significant correlations. This means that most of the interannual variability in ϕ_{LMI} is caused by interannual variability in the genesis latitude, as found in a number of other studies (Kossin et al. 2016; Song and Klotzbach 2018; Daloz and Camargo 2018; Zhao et al. 2022). In the downscaled tracks, only around 20% of the interannual variability in ϕ_{LMI} is a result of changes to $\Delta\phi$, or the TC tracks (Table 1). Of course, these relationships are dependent on coupled atmosphere-ocean interactions in the CESM2 model itself, since the low-level steering flow is responsible for changes in TC track (Wang and Wu 2019).

TABLE 1. Linear Regression between Internal Variability Modes and Variables

Mode	Variable	Slope (°)	r
ENSO	ϕ_{g}	-1.42	0.75
ENSO	ϕ_{LMI}	-1.78	0.75
ENSO	$\Delta\phi$	-0.36	0.50
PDV	ϕ_{g}	-0.66	0.33
PDV	ϕ_{LMI}	-0.86	0.34
PDV	$\Delta\phi$	-0.20	0.27

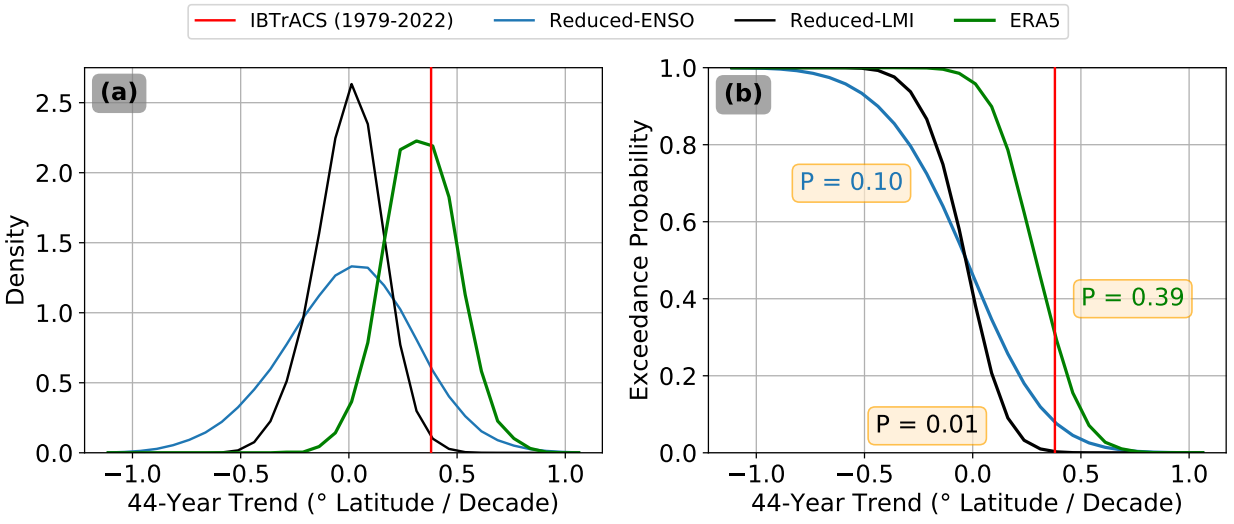

FIG. 3. **(a)** Probability distribution of 44-year trends in the (blue) Reduced-ENSO case, (black) the Reduced-LMI case, (green) the downscaled ERA5 tracks from 1979-2022, and (red) the IBTrACS dataset from 1979-2022. **(b)** Exceedance probability of observing 44-year trends in ϕ_{LMI}. The exceedance probability in the Reduced-ENSO case is 10%, 1% in the Reduced-LMI case, and 39% in the ERA5 downscaled dataset.

4. Forced Trends

A natural next question to ask is what the forced signal in ϕ_{LMI} looks like. This question can be answered by downscaling simulations under historical forcing. However, as recent studies show, coupled models may have biases in the tropical Pacific SST response to increased greenhouse emissions (Coats and Karnauskas 2017; Seager et al. 2019). This has significant ramifications for associated TC risk (Sobel et al. 2023), especially in basins that exhibit strong modulation of TCs by ENSO (as does the Northwest Pacific) (Camargo and Sobel 2005; Camargo et al. 2007a). As we shall show in this section, the biases in the equatorial zonal gradient of tropical Pacific SST have significant implications for modeled/inferred trends in ϕ_{LMI}.

We downscale 6 ensemble members of the CESM2 historical forcing simulations (ensemble members 1 to 6), from 1850-2014, and perform the same ENSO-bias correction as we do for the pre-industrial control runs. This results in a Reduced-ENSO case for each historical simulation ensemble member. We did not create a Reduced-LMI case, in order to directly compare these results with the trends distribution from downscaling ERA5 (which does not employ any bias correction). Using the last 50 years of each simulation (1964-2014), we calculate a distribution of 44-year trends in the annual-average ϕ_{LMI} in the Northwest Pacific. The resulting 44-year trends distribution is thus a function of the historical forcing, the sampling of internal variability by the ensemble members, and the sampling error from the limited number of TCs per year.

Figure 4, in blue, shows the 44-year trends distribution in the Reduced-ENSO case, which exhibits a clear poleward shift in the ϕ_{LMI} distribution, as compared to the trends distribution of the pre-industrial control runs (Figure 3). The mean of the ϕ_{LMI} trends distribution is 0.23° per decade. Note, this is smaller by about 33% than the ϕ_{LMI} trend simulated by the downscaled ERA5 tracks.

What contributes to the poleward trend in ϕ_{LMI}? As shown by Kossin et al. (2014), one potential explanation for the poleward shift of ϕ_{LMI} is an increase in the potential intensity at higher latitudes, and a decrease in potential intensity at lower latitudes (though different reanalyses products disagree about the magnitude of the changes, likely because of spurious changes in upper tropospheric temperature (Vecchi et al. 2013)). They also found a decrease in vertical wind shear at higher latitudes, and an increase in vertical wind shear in the deep tropics.

However, it is not obvious what the relative contributions between internal variability and anthropogenic forcing are to the ϕ_{LMI} trend, especially in light of spatially inhomogeneous warming that may project onto the modes of internal variability. In order to answer this question, we compute another 44-year trends distribution, but in this case, regress out any variability in ϕ_{LMI} that is associated with ENSO, as shown by the black line in Figure 4 and denoted as "No-ENSO". The mean of this distribution represents the ϕ_{LMI} trend due to the component of the forced signal that does not project onto the ENSO index. We also create an analogous distribution but instead regress out the effects of PDV on ϕ_{LMI}.

Immediately obvious is that when regressing out the effect of ENSO, the entire distribution of 44-year trends in ϕ_{LMI} shifts right (stronger poleward trends in ϕ_{LMI}). This is consistent with the facts that 1) the simulated trend in the ENSO index is towards a more loosely "El Niño-like"

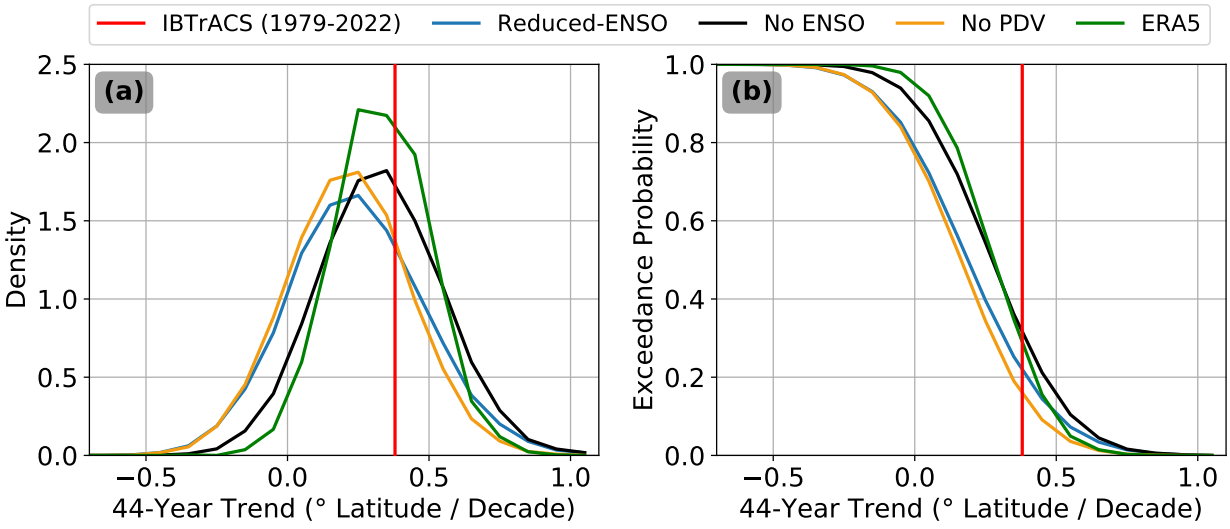

FIG. 4. **(a)** Probability distribution of 44-year trends (using the 1964-2014 window) in the historical CESM2 runs, under the (blue) Reduced-ENSO case. The probability distribution with (black) ENSO and (orange) PDV regressed out of the annual ϕ_{LMI} variations. The trend from the (red) IBTrACS dataset [1979-2022], and trends distribution from downscaling ERA5 over 1979-2022 are shown in red and green, respectively. **(b)** Exceedance probability of observing 44-year trends in ϕ_{LMI}, for all aforementioned cases.

state with enhanced warming in the eastern Pacific, and 2) El Niño events are historically associated with an equatorward shift in TC activity, the opposite of the observed trend. The mean of the ϕ_{LMI} trends distribution increases by around 33% - from 0.23° per decade in the Reduced-ENSO case to 0.32° per decade in the No-ENSO case. Note, this is nearly equal to the mean of the trends distribution obtained by downscaling ERA5, and much closer to the observed trend of 0.38° per decade. This means that the reduced ϕ_{LMI} trend in the historical simulations is likely because CESM2 projects a reduced Pacific SST gradient with warming (more El-Niño-like), in contrast to a strengthening Pacific SST gradient in the observations (more La-Niña-like). Meanwhile, regressing out ϕ_{LMI} variability that is associated with PDV does not have an appreciable effect on the distribution of 44-year trends. This follows from the fact that in the historical forcing simulations, there is an absence of significant trends in the PDV index (not shown).

These results seem to favor anthropogenic forcing, not internal variability, as the root cause of the poleward migration of ϕ_{LMI}. This is because a strongly positive poleward trend in ϕ_{LMI} still exists even when regressing out the effects of (1) ENSO **and** (2) the component of the forced signal that projects onto ENSO. However, as alluded to earlier, the results also suggest that the spatial pattern of warming (the pattern effect) can have significant secondary effects on the poleward migration of ϕ_{LMI}. This follows from the fact that, in a climate model where the equatorial zonal SST gradient weakens with increased greenhouse gas concentrations, regressing out the SST warming that projects onto El Niño patterns significantly shifts the ϕ_{LMI} trends distribution poleward. Now, suppose CESM2 could simulate the observed strengthening of the equatorial zonal gradient. Then we might expect the modeled distribution of ϕ_{LMI} trends to be further to the right than the No-ENSO case. This distribution would then represent a strong poleward trend in TC activity.

5. Conclusions

In this study, we use a recently developed TC downscaling model to understand interannual variability and its control on ϕ_{LMI} in the Northwest Pacific basin. We use the TC model to first downscale ERA5 reanalysis over the historical period (1979-2022), and show that it is able to adequately reproduce the climatology of ϕ_{LMI} in the Northwest Pacific. We then downscale the 1000-year pre-industrial control simulation of the CESM2 model, and show that even in a steady climate, trends in ϕ_{LMI} can occur over short time periods. We create two bias-corrected cases, one which normalizes ENSO variations to be equivalent to that over the historical period, and another which normalizes ϕ_{LMI} variations to the be equivalent over the same period. In these separate cases, there is a 10% and 1% chance, respectively, of observing a ϕ_{LMI} trend larger than that observed. Thus, the results suggest that it is unlikely that natural internal variability is the cause of the observed ϕ_{LMI} trend.

We also downscale 6 ensemble members of the CESM2 historical forcing simulations, to understand how anthropogenic forcing can influence trends in ϕ_{LMI}, and show

that the ϕ_{LMI} trends distribution shifts significantly poleward at least in part as a consequence of anthropogenic forcing. We then regress out any variability that projects onto the ENSO index, and find that the ϕ_{LMI} trends distribution shifts further poleward. These results indicate that there is a rather robust poleward trend in ϕ_{LMI} owing to anthropogenic forcing. They also imply that the spatial pattern of warming has a significant (though secondary) impact on ϕ_{LMI} trends. Given that coupled climate models project a weakening of the equatorial zonal SST gradient (as opposed to the observed strengthening of the gradient), our results suggest that if these same models could properly model TCs, they would also exhibit weaker-than-observed trends in ϕ_{LMI}. This only serves to highlight the criticality of understanding the pattern effect, as there are large implications for TC risk (Sobel et al. 2023).

TC downscaling methods are powerful tools to understand TC behavior in other climates, since TC-resolving grid resolutions are computationally costly for climate time scale simulations (Davis 2018), though recent community efforts such as HighResMIP show promise (Roberts et al. 2020). There are, of course, caveats associated with downscaling methods. Naturally, the climate model simulation has no knowledge of the downscaled TCs, and thus there is no feedback of the TCs onto the climate system. Whether or not this is important is still under debate, but some authors have argued for the role of TCs in modulating the amplitude of ENSO (Li et al. 2023) and the global meridional heat transport (Emanuel 2001; Gutiérrez Brizuela et al. 2023). Furthermore, there are nearly unavoidable model biases when working with climate models, and this is no different with CESM2. For instance, the ϕ_{LMI} distribution for individual storms in the CESM2 simulations (Figure 1d) has a wider distribution than the observations (more storms at low and high latitudes). This is likely a result of biases in the CESM2 mean-state climate, since the ϕ_{LMI} distribution obtained by downscaling ERA5 has little bias compared to the observations when accounting for sampling variability (Figure 1a). While we did our best to mitigate the effects of these biases, at least with regards to the overly-strong amplitude of ENSO, it is difficult to correct the spatial signature of ENSO, among other issues (such as frequency, seasonal climatology, teleconnections, etc.). As a result, the mean and standard deviation of the 44-year trends distributions shown in Figure 3 and 4 are influenced by these biases.

Regardless, compared to existing work, our study offers an alternative approach to disentangling the effect of internal variability and anthropogenic emissions on trends in ϕ_{LMI}. While observational studies looking for global warming signals in TC activity need to remove or smooth out unforced variability, such as ENSO and PDV [see Kossin et al. (2014, 2016); Song and Klotzbach (2018); Zhao et al. (2022)], they implicitly assume that warming does not project onto any modes of interannual variability. The recent observed strengthening of the tropical Pacific SST gradient, which has been interpreted by some authors as a forced signal, muddies interpretation of the short observational TC record. Our work indicates that the interpretation of the poleward trend in TC activity as having a forced component is robust to the uncertainty in the SST pattern effect. At the same time, the pattern effect does significantly affect the magnitude of the trend, and provides another among many motivations to resolve the uncertainty in the structure of forced tropical Pacific warming.

Acknowledgments. JL gratefully acknowledges the support of the National Science Foundation (NSF) through the NSF-AGS Postdoctoral Fellowship, under award number AGS-PRF-2201441. CYL, AHS, and SJC also acknowledge support for this work from NSF, under award number AGS-2217618, and the U.S. Department of Energy (DOE), under award number DE-SC0023333. CYL and SJC also acknowledge additional support from NSF, under award number AGS-2043142.

Data availability statement. The daily ERA5 data for zonal and meridional winds are available through the C3S Climate Data Store via DOI: 10.24381/cds.bd0915c6 (Hersbach et al. 2018)., while the monthly-averaged temperature and specific humidity are available via DOI: 10.24381/cds.6860a573 (Hersbach et al. 2019a). The monthly-mean ERA5 data for sea-surface temperature and surface pressure fields are available through the C3S Climate Data Store via DOI: 10.24381/cds.f17050d7 (Hersbach et al. 2019b). The ERA5 reanalysis data are accessible by creating an account with the Climate Data Store service, and usable according to ECMWF license to use Copernicus products. The CESM2 piControl data are freely available at the ESGF CMIP6 archive via DOI: 10.22033/ESGF/CMIP6.7733 (Danabasoglu et al. 2019b). The CESM2 historical data are also freely available at the ESGF CMIP6 archive via DOI: 10.22033/ESGF/CMIP6.7627 (Danabasoglu et al. 2019a). The IBTrACS data used for evaluation of the model are freely available at NOAA via DOI: 10.25921/82ty-9e16 (Knapp et al. 2018). The TC downscaling model is freely available at `https://github.com/linjonathan/tropical_cyclone_risk` (Lin 2023).

References

Barnston, A. G., M. Chelliah, and S. B. Goldenberg, 1997: Documentation of a highly ENSO-related SST region in the equatorial Pacific. *Atmosphere–Ocean (Canadian Meteorological & Oceanographic Society)*, **35 (3)**.

Camargo, S. J., K. A. Emanuel, and A. H. Sobel, 2007a: Use of a genesis potential index to diagnose ENSO effects on tropical cyclone genesis. *J. Climate*, **20 (19)**, 4819–4834.

Camargo, S. J., A. W. Robertson, S. J. Gaffney, P. Smyth, and M. Ghil, 2007b: Cluster analysis of typhoon tracks. part II: Large-scale circulation and ENSO. *J. Climate*, **20 (14)**, 3654–3676.

Camargo, S. J., and A. H. Sobel, 2005: Western North Pacific tropical cyclone intensity and ENSO. *J. Climate*, **18 (15)**, 2996–3006.

Capotondi, A., C. Deser, A. Phillips, Y. Okumura, and S. Larson, 2020: ENSO and Pacific decadal variability in the Community Earth System Model Version 2. *J. Adv. Earth Syst.*, **12 (12)**, e2019MS002 022.

Chan, J. C., 1985: Tropical cyclone activity in the northwest Pacific in relation to the El Niño/Southern Oscillation phenomenon. *Mon. Wea. Rev.*, **113 (4)**, 599–606.

Chia, H. H., and C. Ropelewski, 2002: The interannual variability in the genesis location of tropical cyclones in the northwest Pacific. *J. Climate*, **15 (20)**, 2934–2944.

Chiang, J. C., and D. J. Vimont, 2004: Analogous Pacific and Atlantic meridional modes of tropical atmosphere–ocean variability. *J. Climate*, **17 (21)**, 4143–4158.

Coats, S., and K. Karnauskas, 2017: Are simulated and observed twentieth century tropical Pacific sea surface temperature trends significant relative to internal variability? *Geophys. Res. Lett.*, **44 (19)**, 9928–9937.

Daloz, A. S., and S. J. Camargo, 2018: Is the poleward migration of tropical cyclone maximum intensity associated with a poleward migration of tropical cyclone genesis? *Climate Dyn.*, **50 (1-2)**, 705–715.

Danabasoglu, G., D. Lawrence, K. Lindsay, W. Lipscomb, and G. Strand, 2019a: NCAR CESM2 model output prepared for CMIP6 CMIP historical. Earth System Grid Federation, URL https://doi.org/10.22033/ESGF/CMIP6.7627, https://doi.org/10.22033/ESGF/CMIP6.7627.

Danabasoglu, G., D. Lawrence, K. Lindsay, W. Lipscomb, and G. Strand, 2019b: NCAR CESM2 model output prepared for CMIP6 CMIP piControl. Earth System Grid Federation, URL https://doi.org/10.22033/ESGF/CMIP6.7733, https://doi.org/10.22033/ESGF/CMIP6.7733.

Danabasoglu, G., and Coauthors, 2020: The community earth system model version 2 (CESM2). *J. Adv. Earth Syst.*, **12 (2)**, e2019MS001 916.

Davis, C., 2018: Resolving tropical cyclone intensity in models. *Geophys. Res. Lett.*, **45 (4)**, 2082–2087.

Emanuel, K., 2001: Contribution of tropical cyclones to meridional heat transport by the oceans. *J. Geophys. Res. Atmos.*, **106 (D14)**, 14 771–14 781.

Emanuel, K., 2006: Climate and tropical cyclone activity: A new model downscaling approach. *J. Climate*, **19 (19)**, 4797–4802.

Emanuel, K., 2017: A fast intensity simulator for tropical cyclone risk analysis. *Natural Hazards*, **88 (2)**, 779–796.

Emanuel, K., R. Sundararajan, and J. Williams, 2008: Hurricanes and global warming: Results from downscaling IPCC AR4 simulations. *Bull. Amer. Meteor. Soc.*, **89 (3)**, 347–368.

Gutiérrez Brizuela, N., M. H. Alford, S.-P. Xie, J. Sprintall, G. Voet, S. J. Warner, K. Hughes, and J. N. Moum, 2023: Prolonged thermocline warming by near-inertial internal waves in the wakes of tropical cyclones. *Proc. Natl. Acad. Sci. (USA)*, **120 (26)**, e2301664 120.

Hersbach, H., 2016: The ERA5 Atmospheric Reanalysis. *AGU Fall Meeting Abstracts*.

Hersbach, H., and Coauthors, 2018: ERA5 hourly data on single levels from 1979 to present. https://doi.org/10.24381/cds.bd0915c6.

Hersbach, H., and Coauthors, 2019a: ERA5 monthly averaged data on pressure levels from 1979 to present. https://doi.org/10.24381/cds.6860a573.

Hersbach, H., and Coauthors, 2019b: ERA5 monthly averaged data on single levels from 1979 to present. *Copernicus Climate Change Service (C3S) Climate Data Store (CDS)*, https://doi.org/10.24381/cds.f17050d7.

Knapp, K., H. Diamond, J. Kossin, M. Kruk, and C. Schreck, 2018: International best track archive for climate stewardship (IBTrACS) project (Version 4). https://doi.org/10.25921/82ty-9e16.

Kossin, J. P., K. A. Emanuel, and S. J. Camargo, 2016: Past and projected changes in western North Pacific tropical cyclone exposure. *J. Climate*, **29 (16)**, 5725–5739.

Kossin, J. P., K. A. Emanuel, and G. A. Vecchi, 2014: The poleward migration of the location of tropical cyclone maximum intensity. *Nature*, **509 (7500)**, 349–352.

Li, H., A. Hu, and G. A. Meehl, 2023: Role of tropical cyclones in determining ENSO characteristics. *Geophys. Res. Lett.*, **50 (6)**, e2022GL101 814.

Lin, I., S. J. Camargo, C.-C. Lien, C.-A. Shi, and J. P. Kossin, 2023a: Poleward migration as global warming's possible self-regulator to restrain future western North Pacific Tropical Cyclone's intensification. *npj Climate and Atmospheric Science*, **6 (1)**, 34.

Lin, J., 2023: linjonathan/tropical_cyclone_risk: Tropical cyclone downscaling. Zenodo, https://doi.org/10.5281/zenodo.7651063.

Lin, J., R. Rousseau-Rizzi, C.-Y. Lee, and A. Sobel, 2023b: An open-source, physics-based, tropical cyclone downscaling model with intensity-dependent steering. *J. Adv. Earth Syst.*, **15 (11)**, e2023MS003 686, https://doi.org/10.1029/2023MS003686.

Mantua, N. J., S. R. Hare, Y. Zhang, J. M. Wallace, and R. C. Francis, 1997: A Pacific interdecadal climate oscillation with impacts on salmon production. *Bull. Amer. Meteor. Soc.*, **78 (6)**, 1069–1080.

Moon, I.-J., S.-H. Kim, P. Klotzbach, and J. C. Chan, 2015: Roles of interbasin frequency changes in the poleward shifts of the maximum intensity location of tropical cyclones. *Environmental Research letters*, **10 (10)**, 104 004.

Rayner, N., D. E. Parker, E. Horton, C. K. Folland, L. V. Alexander, D. Rowell, E. C. Kent, and A. Kaplan, 2003: Global analyses of sea surface temperature, sea ice, and night marine air temperature since the late nineteenth century. *J. Geophys. Res. Atmos.*, **108 (D14)**.

Roberts, M. J., and Coauthors, 2020: Impact of model resolution on tropical cyclone simulation using the HighResMIP–PRIMAVERA multimodel ensemble. *J. Climate*, **33 (7)**, 2557–2583.

Saunders, M., R. Chandler, C. Merchant, and F. Roberts, 2000: Atlantic hurricanes and NW Pacific typhoons: ENSO spatial impacts on occurrence and landfall. *Geophys. Res. Lett.*, **27 (8)**, 1147–1150.

Seager, R., M. Cane, N. Henderson, D.-E. Lee, R. Abernathey, and H. Zhang, 2019: Strengthening tropical Pacific zonal sea surface temperature gradient consistent with rising greenhouse gases. *Nature Climate Change*, **9 (7)**, 517–522.

Sharmila, S., and K. Walsh, 2018: Recent poleward shift of tropical cyclone formation linked to Hadley cell expansion. *Nature Climate Change*, **8 (8)**, 730–736.

Sobel, A. H., and Coauthors, 2023: Near-term tropical cyclone risk and coupled earth system model biases. *Proc. Natl. Acad. Sci. (USA)*, **120 (33)**, e2209631 120.

Song, J., and P. J. Klotzbach, 2018: What has controlled the poleward migration of annual averaged location of tropical cyclone lifetime maximum intensity over the western North Pacific since 1961? *Geophys. Res. Lett.*, **45 (2)**, 1148–1156.

Stevens, B., S. C. Sherwood, S. Bony, and M. J. Webb, 2016: Prospects for narrowing bounds on Earth's equilibrium climate sensitivity. *Earth's Future*, **4 (11)**, 512–522.

Studholme, J., A. V. Fedorov, S. K. Gulev, K. Emanuel, and K. Hodges, 2022: Poleward expansion of tropical cyclone latitudes in warming climates. *Nature Geoscience*, **15 (1)**, 14–28.

Stuecker, M. F., 2018: Revisiting the Pacific meridional mode. *Scientific Reports*, **8 (1)**, 3216.

Vecchi, G. A., S. Fueglistaler, I. M. Held, T. R. Knutson, and M. Zhao, 2013: Impacts of atmospheric temperature trends on tropical cyclone activity. *J. Climate*, **26 (11)**, 3877–3891.

Wang, B., and J. C. Chan, 2002: How strong enso events affect tropical storm activity over the western north pacific. *J. Climate*, **15 (13)**, 1643–1658.

Wang, R., and L. Wu, 2019: Influence of track changes on the poleward shift of LMI location of western North Pacific tropical cyclones. *J. Climate*, **32 (23)**, 8437–8445.

Zhang, W., G. A. Vecchi, H. Murakami, G. Villarini, and L. Jia, 2016: The pacific meridional mode and the occurrence of tropical cyclones in the western north pacific. *J. Climate*, **29 (1)**, 381–398.

Zhao, H., K. Zhao, P. J. Klotzbach, L. Wu, and C. Wang, 2022: Interannual and interdecadal drivers of meridional migration of western North Pacific tropical cyclone lifetime maximum intensity location. *J. Climate*, **35 (9)**, 2709–2722.